Chapter 2
Superfluid-Mott-Insulator Transition

The Hubbard model was originally developed to describe electrons in narrow conduction bands [17]. Its bosonic version, the Bose-Hubbard model [8], yields a very good description of ultracold bosonic atoms trapped in deep optical lattices, as first noted in Ref. [19]. The model shows a phase transition at zero temperature from a superfluid to a Mott-insulating phase, which forms one of the paradigm examples of a quantum phase transition [27]. The transition was first experimentally observed in 2002 using a gas of ultracold ^{87}Rb atoms in a three-dimensional optical lattice [14]. Our presentation is limited to points that are crucial for the understanding of the results presented in this thesis. The chapter also serves as a guide to the remaining thesis. For a more general introduction, see Refs. [4, 8, 27, 35].

2.1 Bose–Hubbard Model

The Bose-Hubbard Hamiltonian is defined as [8]

$$\hat{H}_{\mathrm{BH}} = -J \sum_{\langle i,j \rangle} \hat{b}_j^\dagger \hat{b}_i + \frac{U}{2} \sum_i \hat{n}_i (\hat{n}_i - 1) - \mu \sum_i \hat{n}_i, \tag{2.1}$$

where $\hat{b}_i^\dagger (\hat{b}_i)$ is the boson creation (annihilation) operator on lattice site i, $\hat{n}_i$ is the boson number operator, J is the hopping matrix element, U is the on-site interaction energy, μ is the global chemical potential, and the first sum runs over all nearest neighbors (see also Fig. 2.1). The competition between the terms gives rise to the superfluid-Mott-insulator quantum phase-transition (Fig. 2.1).

In general, quantum phase transitions describe a change in the ground state of a system as the Hamiltonian parameters are varied. Importantly, such transitions occur at zero temperature and are of a purely quantum mechanical nature (in contrast to thermal phase transitions). This can have profound consequences, such as the emergence of quantum correlations (Part II) or the existence of a Higgs amplitude mode (Part III).

M. Endres, *Probing Correlated Quantum Many-Body Systems at the Single-Particle Level*, Springer Theses, DOI: 10.1007/978-3-319-05753-8_2,

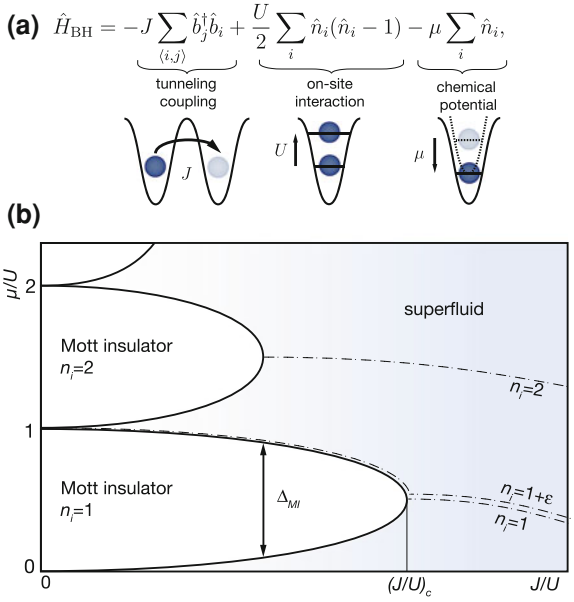

Fig. 2.1 Bose-Hubbard Hamiltonian and phase diagram. **a** Illustration of the three terms in the Bose-Hubbard Hamiltonian (Eq. 2.1). The first term describes hopping between nearest neighboring sites with a hopping rate of $J/\hbar$. Due to the minus sign in front of the positive J, this term favors de-localization of particles. The second term describes pairwise on-site interactions and yields an energy penalty of U for particles sitting on the same lattice site. The third term describes a shift of the on-site energy, which is proportional to the on-site occupation number and the chemical potential μ. Due to the minus sign in front of μ, this term favors higher occupation numbers. **b** Sketch of the zero temperature phase diagram of the Bose-Hubbard model [8]. For small J/U, the system tends to be in a Mott-insulating phase divided into lobes with constant average on-site occupation numbers $n_i = \langle\hat{n}_i\rangle$ (*white* areas). For J/U larger than a critical value $(J/U)_c$, the system is always superfluid (*shaded blue* area) and only lines with constant n_i exist (*dashed lines*). The excitation gap Δ_{MI} in the Mott-insulating phase at constant atom number is given by the width of the Mott-insulating lobes as indicated by the *vertical arrow* for the case $n_i = 1$

2.2 Mott-Insulating and Superfluid States

2.2.1 Mott-Insulating State

2.2.1.1 Atomic Limit

The Mott-insulating state is simplest to understand in the limit of zero tunneling $J/U = 0$, which we will refer to as the atomic limit. In this limit, we can neglect the tunneling term and the ground-state of the system is given by

$$|\Psi\rangle_{J/U=0} \propto \prod_i (\hat{b}_i^\dagger)^{n_i}|0\rangle \propto \prod_i |n_i\rangle. \tag{2.2}$$

This is a tensor product of on-site Fock states $|n_i\rangle$, defined as eigenstates of the on-site boson number operator $\hat{n}_i$, with the on-site occupation numbers n_i as its eigenvalues (Fig. 2.2). Importantly, for the state in Eq. 2.2, the variance $\sigma_i = \langle(\hat{n}_i - \langle\hat{n}_i\rangle)^2\rangle^{1/2}$ of the on-site occupation number vanishes.

We will discuss the physics of this limit in Chap. 4 in more detail. In particular, we will find a step-wise dependence of $n_i(\mu)$ on the chemical potential μ, where $n_i(\mu)$ increases by one at integer values of μ/U and otherwise stays constant. Therefore, the state in Eq. 2.2 shows incompressibility, defined as

$$\frac{\partial\langle\hat{n}_i\rangle}{\partial\mu} = 0, \tag{2.3}$$

for non-integer values of μ/U.

2.2.1.2 Number Fluctuations and Incompressibility

The ground state in the Mott-insulating regime is only given by Eq. 2.2 at $J/U = 0$, and in general Mott-insulating states have a more complicated structure. Particularly, a small tunneling coupling J leads to the emergence of quantum correlated particle-hole pairs, which we directly observed in the experiment (Chap. 5). The effect of this is to introduce correlated number-fluctuations in the system, which lead to non-vanishing on-site fluctuations $\sigma_i > 0$. Especially in low-dimensional systems, these number fluctuations take on significant values already in the Mott-insulating regime. Indeed, it should be stressed that the defining property of Mott insulators is incompressibility as defined in Eq. 2.3 and not $\sigma_i = 0$ [4].

2.2.1.3 Excitation Structure

In general, we find a Mott-insulating state only at integer filling, i.e., the average on-site occupation $\langle\hat{n}_i\rangle$ equals a non-zero integer (see dashed lines in Fig. 2.1). Additional particles that are added to the system can move (almost freely) on top of the Mott-insulating background and form a (quasi-)condensate state [4, 8]. The same phenomenon appears when removing particles from a Mott state, leading to a condensation of holes. Thus, any deviation from integer filling immediately leads to a superfluid state.

Adding (removing) a single particle to a Mott-insulating state is associated with a finite energy cost. This energy gap is non-zero for all J/U and μ values in a given Mott lobe and vanishes at the boundaries of the lobes. Therefore, the ground state within a given lobe has always the same total atom number, independent of μ. Because of the translational invariance of the system, we also find that the average occupation number is independent of μ, thus the state is incompressible $\frac{\partial\langle\hat{n}_i\rangle}{\partial\mu} = 0$. We therefore find that incompressibility is a direct consequence of the finite excitation gap for adding (removing) a single particle.

The excitation gap can be directly read off from the phase diagram. At a fixed J/U and μ/U, the gap for adding (removing) a particle is given by the distance to the upper (lower) Mott boundary [8].

Additionally, we are interested in excited states at a constant total atom number. Such states are the result of a simultaneous creation of an extra particle and a hole. The corresponding excitation gap Δ_{MI} at fixed J/U is given by the full width of the Mott lobe in μ direction [18] (see arrow in Fig. 2.1). The gap Δ_{MI} also sets the energy scale for thermal activation of defects in the Mott-insulating regime [8].

Increasing J/U, the width of the Mott lobe gradually shrinks and therefore the excitation gap Δ_{MI} is reduced until it finally closes at $J/U = (J/U)_c$, an effect that we could directly observe experimentally (Sect. 9.2). This behavior can be intuitively understood as follows. At finite tunneling, an added particle (hole) can decrease its kinetic energy by de-localizing over the entire system. The energy reduction becomes larger with increasing J. At $J/U > (J/U)_c$, the energy reduction of a combined particle and hole excitation, due to de-localization, overcompensates the energy cost due to the interaction term.

2.2.1.4 Order Parameters

Following the previous discussion, a suitable order parameter for the Mott-insulating regime can be formulated based on the excitation gap Δ_{MI} or the compressibility $\frac{\partial \langle \hat{n}_i \rangle}{\partial \mu}$. With this, however, one makes use of the excited state structure or a response property. It is interesting to ask if there is a suitable order parameter which depends only on the structure of the ground state (at fixed J/U and μ). In Chap. 6, we will show that this is the case for one-dimensional systems where the order parameter can be based on non-local correlation functions that we directly observed experimentally. We will present an extension of this concept to two-dimensional systems in Chap. 7.

2.2.2 Superfluid State

2.2.2.1 Non-interacting Limit

The superfluid phase is easiest to discuss starting from the non-interacting limit $U/J = 0$. Neglecting the interaction term, the ground state is given by

$$|\Psi\rangle_{U/J=0} \propto \left(\sum_i \hat{b}_i^\dagger \right)^N |0\rangle, \tag{2.4}$$

where N denotes the total number of particles. The state in Eq. 2.4 shows Bose-Einstein condensation in the zero-momentum Bloch state, which has a creation operator proportional to $\sum_i \hat{b}_i^\dagger$ (Sect. 2.4). In this single particle state, an atom is de-localized over the entire lattice (Fig. 2.2).

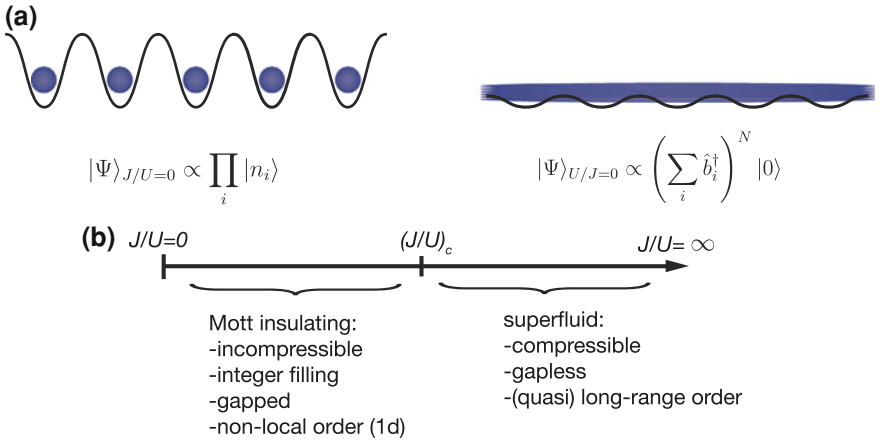

Fig. 2.2 Illustration of states in the atomic/non-interacting limit and properties of the Mott-insulating/superfluid phase. **a** Sketch of the onsite-number distribution in the atomic limit ($J/U = 0$, *left*) and the non-interacting limit ($U/J = 0$, *right*). In the atomic limit, the atoms are strongly localized and the many-body wave function is given by a product of on-site Fock states (Eq. 2.2). In the non-interacting limit, each atom is delocalized over the entire lattice, and the many-body wave function is a product of delocalized single-particle states (Eq. 2.4). For intermediate J/U, the ground states have a more complicated structure (see text). **b** Summary of the main properties of Mott-insulating and superfluid states

In the thermodynamic limit, the state in Eq. 2.4 becomes indistinguishable to a product of coherent states [4]

$$|\Psi\rangle_{U/J=0} \propto \prod_i |\alpha_i\rangle. \tag{2.5}$$

The on-site coherent state $|\alpha_i\rangle$ is defined as an eigenstate of the destruction operator $\hat{b}_i$ with complex eigenvalue α_i [12]. The average on-site occupation number is given by $\langle \hat{n}_i \rangle = |\alpha_i|^2$ and we find a Poisson probability distribution to observe a certain on-site occupation number. This leads to large on-site number fluctuations $\sigma_i^2 = \langle \hat{n}_i \rangle$.

The state in Eq. 2.5 shows off-diagonal long-range order, defined as (see, e.g., [23])

$$\lim_{|i-j|\to\infty} G^{(1)}(i, j) = \lim_{|i-j|\to\infty} \langle \hat{b}_i^\dagger \hat{b}_j \rangle \neq 0, \tag{2.6}$$

where $G^{(1)}(i, j) = \langle \hat{b}_i^\dagger \hat{b}_j \rangle$ is the single-particle density matrix. $G^{(1)}(i, j)$ is experimentally accessible using time-of-flight imaging [4], which was used in Ref. [14] to detect the superfluid-Mott-insulator transition in a three-dimensional system.

2.2.2.2 Superfluidity and Long-Range Order

At finite interactions $U/J > 0$, the superfluid state is, in general, more complicated than the ideal Bose-Einstein condensation state in Eq. 2.4. Finite interactions lead, e.g., to a reduction of number-fluctuations, such that $\sigma_i^2 < \langle \hat{n}_i \rangle$ already in the superfluid phase. Additionally, we would like to stress that the defining quality of the superfluid state is not long-range order (or Bose-Einstein condensation), but a non-vanishing superfluid density n_{SF}, when the total density of the system is written as $n = n_{SF} + n_n$, where n_n is the normal component. In particular, for low-dimensional systems, long-range order in the above sense is replaced by quasi-long-range order, defined as an algebraic decay of $G^{(1)}(i, j)$. For a discussion of the relation between the behavior of $G^{(1)}(i, j)$ and superfluidity, see Refs. [4, 23].

2.2.2.3 Excitation Structure

In contrast to the Mott-insulating phase, the superfluid phase, in the thermodynamic limit, does not have a finite excitation gap, i.e. it is gapless [4, 8, 24, 27]. The corresponding low energy excitations are Nambu-Goldstone modes that show a linear, phonon-like dispersion relation at low momenta. In general, an excitation of these modes leads to currents of the total density n.

In a strongly interacting superfluid, however, additional Higgs amplitude modes, which have a non-vanishing excitation gap, can appear (Part III). In contrast to Nambu-Goldstone modes, such modes lead to variations of the superfluid density n_{SF} at an almost constant overall density n [18]. Similar to the excitation gap of the Mott-insulating phase, the gap to Higgs modes closes approaching the phase transition, an effect that we could directly observe experimentally (Sect. 9.2).

2.3 Phase Transitions in the Bose–Hubbard Model

The Bose-Hubbard model features different types of phase transitions. In particular, we find a quantum phase transition varying J/U and μ, but the system can also go from a superfluid to a normal phase as the temperature T is increased. We will first discuss the $T = 0$ transition.

At $T = 0$ one can cross the superfluid-Mott-insulator boundary in different ways. First, the boundary can be crossed at constant integer density, going through the tip of the Mott lobe by varying J/U (tip of lobe transition). Or, in contrast, one can vary the chemical potential at a constant J/U, inducing a transition that is accompanied by a change in density (generic transition). The tip of the lobe transition is special in the sense that the low-energy physics close to the transition point is described by an effectively relativistic theory [27]. The emergence of a Higgs mode in a strongly interacting superfluid close to the tip of lobe transition can be directly understood within this framework (Chap. 8). Concerning the generic transition, we already argued that an addition of particles (holes) to the Mott state with integer filling leads to a condensation of the added particles (holes). Consequently, we will

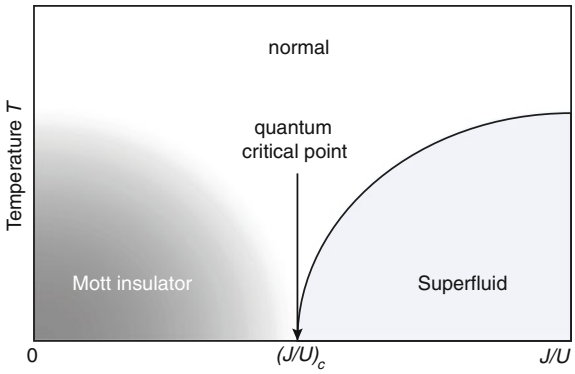

Fig. 2.3 Phase diagram at finite temperature. Figure shows a sketch of the phase diagram of the Bose-Hubbard model at constant, integer filling as a function of J/U and the temperature T [29]. For $J/U > (J/U)_c$, the system is in a superfluid phase for temperatures below a critical temperature (*solid line*), which shows a characteristic reduction close to $(J/U)_c$. For higher temperatures, we find a normal phase, which is continuously connected to the Mott-insulating phase for $J/U < (J/U)_c$. The point at $T = 0$ and $J/U = (J/U)_c$ defines a tricritical point

see in Chap. 8 that the dynamics close to the phase boundary is essentially described by a time-dependent Gross-Pitaevskii equation.

We now turn to a description at finite $T > 0$. In Fig. 2.3, we plot the phase diagram as a function of J/U and T at a constant integer density [27]. For low temperatures and $J/U > (J/U)_c$, we find a superfluid phase. Increasing T, the system passes through a thermal phase transition to a normal phase. The critical temperature for this transition shows a characteristic reduction close to $(J/U)_c$, which has been observed experimentally in Ref. [29]. Additionally, we find that the point at $T = 0$ and $J/U = (J/U)_c$ defines a tricritical point, connected to the Mott-insulating, superfluid and normal phase.

There is no sharp phase boundary between the Mott-insulating and normal phase. Indeed, strictly speaking, the Mott-insulating state only exists at $T = 0$, since for $T > 0$ we always find a finite compressibility. However, for temperatures $T \ll \Delta_{MI}/k_B$ (k_B, Boltzman constant), the thermal activation of defects is strongly suppressed and characteristic properties of the Mott-insulating phase can still be observed [10]. For further details concerning the properties of the quantum phase transition, see Ref. [27].

We finish our discussion by stating the known critical values $(J/U)_c$ for a square lattice as a function of the dimensionality of the system in Table 2.1. In low-dimensional systems, the Mott-insulating phase reaches to higher J/U values. This effect is stronger than anticipated by a mean-field approximation [8], which yields $(\frac{J}{U})_{c,MF} \approx \frac{1}{z\,5.8}$, where z is the number of nearest neighbors.

Table 2.1 Critical value $(J/U)_c$ for the superfluid-Mott-insulator transition

	$d=3$	$d=2$	$d=1$
$(J/U)_c \approx$	0.034 [5]	0.059 [6]	0.3 [20, 22]
$(J/U)_{c,MF} \approx \frac{1}{z\,5.8} \approx$	0.029	0.043	0.086

Top row critical values $(J/U)_c$, based on numerical calculations for the transition in dimensions $d = 3, 2, 1$. *Bottom row* same as *top row*, but based on a mean-field calculation. The mean-field values underestimate $(J/U)_c$, particularly for $d = 2, 1$

2.4 Realization of the Bose–Hubbard Model in Optical Lattices

We give a short introduction on how the Bose-Hubbard model can be realized with ultracold alkali atoms in an optical lattice. Very detailed descriptions can be found in Refs. [4, 9, 13, 31, 34]. As the three-dimensional lattice potential, in our case, is separable, we first deal with a single lattice axis. The full solution is a simple extension of these results (Sect. 2.4.3).

The starting point of our discussion is the general many-body Hamiltonian

$$\hat{H} = \int dx \hat{\Psi}^\dagger(x) \left(-\frac{\hbar^2}{2m}\frac{\partial^2}{\partial x^2} + V_l(x) - \mu \right) \hat{\Psi}(x) + \frac{1}{2}\int dx dx' \hat{\Psi}^\dagger(x)\hat{\Psi}^\dagger(x')V(x-x')\hat{\Psi}(x')\hat{\Psi}(x) \tag{2.7}$$

for spinless bosons interacting via $V(x - x')$ in the presence of an external potential $V_l(x)$ (see, e.g., Ref. [1]). $\hat{\Psi}^\dagger(x)(\hat{\Psi}(x))$ are creation (annihilation) operators at position x, with commutation relations $[\hat{\Psi}(x), \hat{\Psi}^\dagger(x')] = \delta(x - x')$.

2.4.1 Optical Lattice Potential

An optical lattice, in its simplest form, is created by a pair of counter-propagating laser beams with the same laser wavelength λ_L. This leads to a standing wave along the propagation direction, which has a periodically varying intensity profile $I(x)$ proportional to $\cos(k_{\text{lat}}x)$, where $k_{\text{lat}} = \frac{2\pi}{a_{\text{lat}}}$ and $a_{\text{lat}} = \lambda_L/2$ (Fig. 2.4).

The lattice light creates a conservative potential $V_l(x)$ for the atoms via the dynamical Stark effect (or a.c. Stark effect). A comparison of different treatments for this effect can be found in Ref. [16]. For alkali atoms, the potential $V_l(x)$ resulting from linearly polarized light and detunings that do not resolve the hyperfine structure is [15]

$$V_{\text{L}}(x) = -\frac{\pi c^2}{2\omega_{\text{D2}}^3}\frac{1}{\tau_{\text{D2}}}\left(\frac{2}{\Delta_{\text{D2}}} + \frac{1}{\Delta_{\text{D1}}}\right) I(x), \tag{2.8}$$

where c is the speed of light and τ_{D2} is the lifetime of the excited state of the D2 transition. The effective detunings $\Delta_{D1/D2}$ are given by

$$\frac{1}{\Delta_{\mathrm{D1/D2}}} = \frac{1}{(\omega_{\mathrm{D1/D2}} - \omega_L)} + \frac{1}{(\omega_{\mathrm{D1/D2}} + \omega_L)}, \tag{2.9}$$

with $\omega_L = 2\pi \frac{c}{\lambda_L}$ and $\omega_{\mathrm{D1/D2}} = 2\pi \frac{c}{\lambda_{\mathrm{D1/D2}}}$, where $\lambda_{\mathrm{D1/D2}}$ is the transition wavelength of the D1 (D2) line respectively.

The resulting potential $V_L(x)$ is proportional to $\pm I(x)$, for effective blue (red) detuning, i.e. the term $\frac{2}{\Delta_{\mathrm{D2}}} + \frac{1}{\Delta_{\mathrm{D1}}}$ is negative (positive). We thus find a periodic lattice potential

$$V_l(x) = \pm \frac{V_0}{2} \cos\left(k_{\mathrm{lat}} x\right), \tag{2.10}$$

where we have appropriately chosen an absolute energy offset and the overall phase of the periodic potential. For blue (red) detuning, the minima of $V_l(x)$ coincide with the minima (maxima) of the intensity distribution $I(x)$. V_0 is the full lattice depth, which is typically stated in units of the lattice recoil energy $E_r = h^2/(8ma_{\mathrm{lat}}^2)$, where m is the atomic mass. In the case of ^{87}Rb and $\lambda_L = 1{,}064$ nm, we find $E_r/h \approx 2$ kHz.

2.4.2 Derivation of the Tunneling and Interaction Term

2.4.2.1 Tunneling Term

The energy eigenstates of the single-particle Hamiltonian $\hat{H}_s = -\frac{\hbar^2}{2m}\frac{\partial^2}{\partial x^2} + V_l(x)$, with $V_l(x)$ defined in Eq. 2.10, are Bloch functions $\Phi_q(x)$ with eigenenergies $\epsilon(q)$, where q is a quasi-momentum $|q| < \frac{\pi}{a_{\mathrm{lat}}}$ restricted to the first Brillouin zone (Fig. 2.4). For an introduction to periodic potentials, we refer to Ref. [2]. We will restrict ourself to the lowest Bloch band and suppress a band index.

The Bloch functions $\Phi_q(x)$ and the eigenenergies $\epsilon(q)$ can, in general, be calculated with a numerical band-structure calculation [13]. Alternatively, one can show that the eigenvalue equation $\hat{H}_s \Psi(x) = E\Psi(x)$ is equivalent to the Mathieu equation, which has Mathieu cosine and Mathieu sine functions as its unique even and odd solutions [25]. Following Ref. [21], one can write the Bloch functions $\Phi_q(x)$ as a linear combination of the latter functions.

The key concept for the derivation of the Bose-Hubbard model is the Wannier function $w_i(x)$, defined by a Fourier transform of the Bloch functions [32]

$$w_i(x) = \frac{1}{\sqrt{N_l}} \sum_q \Phi_q(x) e^{-iqx_i}, \tag{2.11}$$

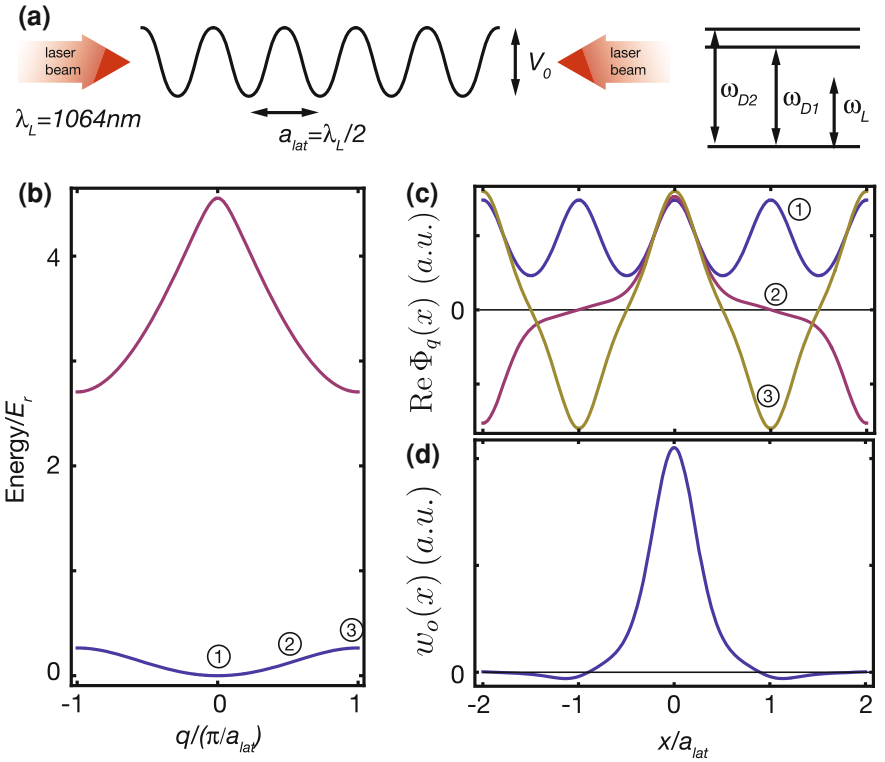

Fig. 2.4 Realizing the Bose-Hubbard model using optical lattices. **a** Illustration of an optical lattice potential. Two counter-propagating laser beams with wavelength λ_L interfere, and form a standing wave with period $a_{lat} = \lambda_L/2$. The laser frequency $\omega_L = 2\pi\frac{c}{\lambda_L}$ is chosen to be far off-resonant to the D1 and D2 lines, resulting in an conservative trapping potential due to the dynamical Stark effect. **b** Band structure for a lattice depth of $V_0 = 5E_r$ including the lowest (*blue*) and the first excited (*red*) band. **c** Real part of the Bloch wave functions $\Phi_q(x)$ for the lowest band for quasi-momenta $q = 0, \pi/(2a_{\mathrm{lat}}), \pi/a_{\mathrm{lat}}$ (*blue*, *red*, *yellow*; see corresponding numbers in **b**). **d** Wannier function of the lowest band $w_0(x) \propto \sum_q \Phi_q(x)$ for the central lattice site at $x_i = 0$. The summation of Bloch wave functions with different momenta leads to a constructive interference around $x = 0$ and to a destructive interference at neighboring lattice sites. The Wannier function is completely real, because the imaginary parts of $\Phi_q(x)$ destructively interfere at all positions (not shown)

where x_i refers to a lattice site i, defined by the minima of the lattice potential $V_l(x)$. The sum runs over the first Brillouin zone and N_l is the number of lattice sites.

The Wannier functions $w_i(x)$ of the lowest band have the following important properties. First, they are only functions of the distance $x - x_i$. Additionally, they can be chosen to be symmetric around x_i and to be real [21]. Furthermore, they form a complete, orthogonal set for the lowest band. For sufficiently deep lattices, they are strongly localized around x_i (Fig. 2.4).

The crucial step in the derivation of the Bose-Hubbard model is the expansion of the boson creation (annihilation) operators in terms of Wannier functions given by

$$\hat{\Psi}^\dagger(x) = \sum_i w_i^*(x)\hat{b}_i^\dagger \tag{2.12}$$

$$\hat{\Psi}(x) = \sum_i w_i(x)\hat{b}_i, \tag{2.13}$$

where $\hat{b}_i^\dagger$ ($\hat{b}_i$) are the creation (annihilation) operators for a state with Wannier wave function $w_i(x)$.

Due to the completeness of $w_i(x)$, $\hat{b}_j$ and $\hat{b}_i^\dagger$ fulfill the commutation relations

$$[\hat{b}_i, \hat{b}_j^\dagger] = \delta_{i,j}. \tag{2.14}$$

With Eq. 2.13, we can write the non-interacting part $\hat{H}_0$ of $\hat{H}$ as

$$\begin{aligned}\hat{H}_0 &= \int dx \hat{\Psi}^\dagger(x)\left(-\frac{\hbar^2}{2m}\frac{\partial^2}{\partial x^2} + V_l(x) - \mu\right)\hat{\Psi}(x) \\ &= -\sum_{i\neq j} J_{i,j}\,\hat{b}_i^\dagger\hat{b}_j - \sum_i(\mu + J_{i,i})\hat{b}_i^\dagger\hat{b}_i \\ &= -\sum_{i\neq j} J_{i,j}\,\hat{b}_i^\dagger\hat{b}_j - \mu\sum_i \hat{b}_i^\dagger\hat{b}_i. \end{aligned} \tag{2.15}$$

In the last line, we absorbed $J_{i,i}$ in the chemical potential μ, by replacing $\mu \rightarrow \mu - J_{i,i}$. The tunneling matrix element $J_{i,j}$ is given by

$$J_{i,j} = -\int dx\, w_i^*(x)\left(-\frac{\hbar^2}{2m}\frac{\partial^2}{\partial x^2} + V_l(x)\right) w_j(x). \tag{2.16}$$

The first term in Eq. 2.15 describes hopping between arbitrary lattice sites with hopping matrix element $J_{i,j}$. In deep lattices, $J_{i,j}$ is negligible for all, but nearest neighbors. Defining $J = J_{i,i+1}$ and neglecting all other $J_{i,j}$, we arrive at

$$\hat{H}_0 \approx -J\sum_{\langle i,j\rangle}\hat{b}_i^\dagger\hat{b}_j - \mu\sum_i \hat{b}_i^\dagger\hat{b}_i \tag{2.17}$$

resembling the non-interacting terms in the Bose-Hubbard model.

2.4.2.2 Interaction Term

At sufficiently low temperatures, interactions between bosonic alkali atoms are restricted to s-wave collisions. The scattering wavefunction, resulting from the true interaction potential, is at low collisional momenta correctly reproduced by a delta function contact potential [4, 7, 26]

$$V(\vec{r}-\vec{r}') = \frac{4\pi\hbar^2 a_s}{m}\delta(\vec{r}-\vec{r}') = g\,\delta(\vec{r}-\vec{r}'). \tag{2.18}$$

The s-wave scattering length a_s takes on a value $a_s = 100.4(1)\,a_B$ ($a_B \approx 5.29 \times 10^{-11}$ m, the Bohr radius) for collisions between ^{87}Rb atoms in the hyperfine state $5S_{1/2}$, $F = 1, m_F = -1$ used in our experiments [30]. The interaction strength is defined as $g = \frac{4\pi\hbar^2 a_s}{m}$. We do not discuss additional regularization terms [7].

We would like to deal with a single lattice axis first, but the previous formula defines the interaction potential in three dimensions. To be formally correct and to yield the right units, we define a one-dimensional interaction potential $V_{1\mathrm{d}}(x-x') = g_{1\mathrm{d}}\,\delta(x-x')_{1\mathrm{d}}$, with a one-dimensional interaction strength $g_{1\mathrm{d}} = g\cdot(\int dx\,|w_i(x)|^4)^2$ and a one-dimensional delta function $\delta(x-x')_{1\mathrm{d}}$. We will deal with the full three-dimensional problem in the next subsection and the factor $(\int dx\,|w_i(x)|^4)^2$ will be motivated there.

With this at hand, we can write the interaction part $\hat{H}_I$ of $\hat{H}$ as

$$\begin{aligned}\hat{H}_I &= \frac{1}{2}\int dx dx' \hat{\Psi}^\dagger(x)\hat{\Psi}^\dagger(x')V(x-x')_{1\mathrm{d}}\hat{\Psi}(x')\hat{\Psi}(x)\\ &= \frac{g_{1\mathrm{d}}}{2}\int dx \hat{\Psi}^\dagger(x)\hat{\Psi}^\dagger(x)\hat{\Psi}(x)\hat{\Psi}(x)\end{aligned} \tag{2.19}$$

Inserting the expansion in terms of Wannier functions (Eq. 2.13) yields

$$\begin{aligned}\hat{H}_I &\approx \frac{U}{2}\hat{b}_i^\dagger\hat{b}_i^\dagger\hat{b}_i\hat{b}_i\\ &= \frac{U}{2}\hat{b}_i^\dagger\hat{b}_i(\hat{b}_i^\dagger\hat{b}_i - 1),\end{aligned} \tag{2.20}$$

with the on-site interaction U given by

$$U = g_{1\mathrm{d}}\int dx\,|w_i(x)|^4. \tag{2.21}$$

In the first line of Eq. 2.20, we assumed that $|\int dx\,|w_i(x)|^4| \gg |\int dx\,w_k(x)w_l(x)w_m(x)w_n(x)|$, if at least one of the indices k, l, m, n differs from the others. This is justified, when the Wannier functions are strongly localized and the overlap between neighboring sites is therefore small.

2.4.3 Three-Dimensional Optical Lattice and Harmonic Confinement

A three-dimensional optical lattice, in our case, is created by three pairs of counter-propagating laser beams intersecting at right angles (Chap. 3). All beams are chosen

to have the same laser wavelength and the overall potential thus resembles a simple cubic lattice.

Additionally, all beams have an intrinsic Gaussian beam shape, which can be approximated by a harmonic potential in the beam's center. The overall lattice potential can be written as [13]

$$V_l(\vec{r}) \approx V_p(\vec{r}) + V_h(\vec{r}) \tag{2.22}$$

$$V_p(\vec{r}) = \pm\left(\frac{V_x}{2}\cos\left(k_{\text{lat}}r_x\right) + \frac{V_y}{2}\cos\left(k_{\text{lat}}r_y\right) + \frac{V_z}{2}\cos\left(k_{\text{lat}}r_z\right)\right) \tag{2.23}$$

$$V_h(\vec{r}) = \pm\left(\frac{1}{2}m\omega_x^2 r_x^2 + \frac{1}{2}m\omega_y^2 r_y^2 + \frac{1}{2}m\omega_z^2 r_z^2\right), \tag{2.24}$$

where $\vec{r} = (r_x, r_y, r_z)$ is the position, V_x, V_y, V_z are the full lattice depths in x, y, z-directions and $\omega_x, \omega_y, \omega_z$ are the trapping frequencies in x, y, z-directions. We therefore find a separable periodic potential $V_p(\vec{r})$ and a harmonic potential $V_h(\vec{r})$.

The previous one-dimensional calculation is easily extended to the three-dimensional case. The band structure calculation for each axis yields Wannier functions $w_i^x(r_x)$, $w_i^y(r_y)$, $w_i^z(r_z)$ for the x, y, z axis respectively. Since the periodic potential is separable, the Wannier function $w_i(\vec{r})$ for the three-dimensional case is given by

$$w_i(\vec{r}) = w_i^x(r_x)w_i^y(r_y)w_i^z(r_z), \tag{2.25}$$

which replaces $w_i(x)$ in the above calculation.

In total, we find

$$\hat{H} \approx -\sum_{\langle i,j\rangle} J_\alpha \hat{b}_i^\dagger \hat{b}_j + \frac{U}{2}\sum_i \hat{n}_i(\hat{n}_i - 1) - \sum_i \mu_i \hat{b}_i^\dagger \hat{b}_i, \tag{2.26}$$

where we absorbed the terms resulting from the harmonic potential $V_h(\vec{r})$ in a local chemical potential μ_i given by

$$\mu_i = \mu - V_h(\vec{r_i}). \tag{2.27}$$

The resulting model in Eq. 2.26 is usually treated in a local density approximation, which assumes that the solution in the homogeneous case at a given constant $\tilde{\mu}$ reproduces the local physics in the spatially varying problem at $\mu_i = \tilde{\mu}$ (see, e.g., Ref. [33] for a discussion). This treatment becomes exact in the atomic limit (Chap. 4).

Additionally, we introduced a hopping matrix element J_α along the different axes, where $\alpha = x$, y or z depending on whether the nearest neighbors i, j are aligned in x, y or z direction, respectively. The hopping matrix element J_α is given by

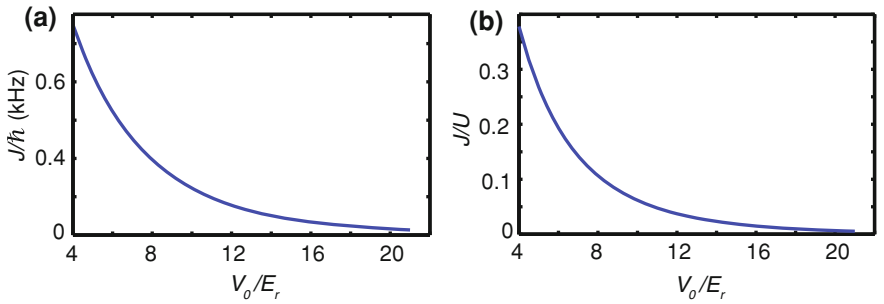

Fig. 2.5 Bose-Hubbard parameters as a function of the lattice depth. Bose-Hubbard parameters as a function of the lattice depth V_0 in units of the lattice recoil energy E_r. **a** The plot shows that J falls off approximately exponentially with the lattice depth V_0. **b** The behavior of J/U is dominated by the strong dependence of J on V_0. For the calculation of J/U shown in this plot, we kept the depths of the two orthogonal axes constant at $17E_r$ and $20E_r$ resembling the situation described in Sect. 5.2. For the calculation, we used $a_{\text{lat}} = 532$ nm

$$J_\alpha = -\int dr_\alpha \, w_i^\alpha(r_\alpha)^* \left(-\frac{\hbar^2}{2m}\frac{\partial^2}{\partial r_\alpha^2} + \frac{V_\alpha}{2}\cos\left(k_{\text{lat}} r_\alpha\right)\right) w_{i+1}^\alpha(r_\alpha) \tag{2.28}$$

$$= \frac{1}{N_l}\sum_{|q|<\frac{\pi}{a_{\text{lat}}}} e^{iqa_{\text{lat}}}\epsilon^\alpha(q), \tag{2.29}$$

where in the last line, we inserted the definition of the Wannier functions (Eq. 2.13) and used the fact that the Bloch functions are eigenstates of $-\frac{\hbar^2}{2m}\frac{\partial^2}{\partial r_\alpha^2} + \frac{V_\alpha}{2}\cos\left(k_{\text{lat}} r_\alpha\right)$ with eigenvalues $\epsilon^\alpha(q)$.

The on-site interaction U is given by

$$U = g\int dr_x \, |w_i^x(r_x)|^4 \int dr_y \, |w_i^y(r_y)|^4 \int dr_z \, |w_i^z(r_z)|^4. \tag{2.30}$$

In Fig. 2.5, we show J and U, determined from the previous formulas using a band-structure calculation for typical experimental parameters.

Finally, we discuss that the definition of the Wannier functions is to some degree ambiguous. The problem lies in the fact that the Bloch wavefunctions can be multiplied by a q dependent phase factor, such that $\Phi_q(x) \to e^{i\phi(q)}\Phi_q(x)$, which does not change their properties. However, the phase factor enters the Fourier transform used for the definition of the Wannier function in Eq. 2.11 and, in general, changes the resulting Wannier function.

In practice, one is interested in Wannier functions, which are maximally localized at a single lattice site. The conditions for maximally localized Wannier functions for general one-dimensional periodic potentials have been investigated in Ref. [21]. In our case, to yield maximally localized Wannier functions for the lowest band, the phases for the Bloch functions have to be fixed such that

$$\Im(e^{i\phi(q)}\Phi_q(0)) = 0, \tag{2.31}$$

where $\Im$ denotes the imaginary part.

From Eq. 2.29, we see that this does not affect the value of the tunneling matrix element as only the band-structure enters the formula. In contrast, the on-site interaction does depend on the choice of the phase factor (Eq. 2.30).

2.4.4 Discussion

Here we summarize the assumptions that led to the derivation of Eq. 2.26 and verify that they are justified for the experimental values in this thesis.

First, we restricted ourself to the lowest Bloch band, which is justified if the thermal and interaction energies are smaller than the band gap (Fig. 2.4). Typical interaction energies, in our case, are about $U/h \approx 500$ Hz and we find temperatures $T \ll U/k_b$ (Chap. 4). Both energies are therefore significantly smaller than the band gap of about 4–16 kHz for our typical lattice depths of about 4–21 E_r.

Additionally, we only accounted for nearest neighbor tunneling, i.e., we made a tight-binding approximation. For our typical lattice depths, the tunneling matrix element to the next-nearest neighbor is about a factor of 10–1,000 smaller than the one for nearest neighbor tunneling and the assumption is therefore legitimate.

Furthermore, we assumed pure on-site interactions, which is justified in our case because nearest-neighbor interactions are suppressed by at least a factor of 200.

Finally, the on-site interaction U might show a small dependence on the on-site occupation number that we neglected (see, e.g., Ref. [34] for a discussion).

The main control knobs in our experiment are the lattice depths V_x, V_y, V_z, which can be tuned to reach different Bose-Hubbard parameters J_x, J_y, J_z and U. In this section, we showed that these parameters can be determined from knowledge of the band structure including the Bloch waves $\Phi_q(x)$ with eigenenergies $\epsilon(q)$. The band structure can be easily numerically calculated after the lattice depths V_x, V_y, V_z have been determined experimentally (Appendix A).

In conclusion, we find an exceptional situation where the many-body Hamiltonian is known, and the Hamiltonian parameters can be controlled and determined with a high degree of accuracy.

References

1. Altland A, Simons B (2006) Condensed matter field theory. Cambridge University Press, Cambridge. ISBN 0521845084
2. Ashcroft NW, Mermin ND (1976) Solid state physics. Saunders, Philadelphia. ISBN 0030839939

3. Bakr WS, Peng A, Tai ME, Ma R, Simon J, Gillen JI, Fölling S, Pollet L, Greiner M (2010) Probing the superfluid-to-Mott insulator transition at the single-atom level. Science 329:547–550
4. Bloch I, Dalibard J, Zwerger W (2008) Many-body physics with ultracold gases. Rev Mod Phys 80:885–964
5. Capogrosso-Sansone B, Prokof'ev N, Svistunov B (2007) Phase diagram and thermodynamics of the three-dimensional Bose-Hubbard model. Phys Rev B 75:134302
6. Capogrosso-Sansone B, Söyler S, Prokof'ev N, Svistunov B (2008) Monte Carlo study of the two-dimensional Bose-Hubbard model. Phys Rev A 77:015602
7. Dalibard J (1999) Collisional dynamics of ultra-cold atomic gases. In: Proceedings of the International School of Physics-Enrico Fermi, vol 321
8. Fisher MPA, Weichman PB, Grinstein G, Fisher DS (1989) Boson localization and the superfluid-insulator transition. Phys Rev B 40:546–570
9. Fölling S (2008) Probing strongly correlated states of ultracold atoms in optical lattices. PhD thesis, Johannes-Gutenberg-Universität Mainz, Mainz
10. Gerbier F (2007) Boson Mott insulators at finite temperatures. Phys Rev Lett 99:120405
11. Gerry C, Knight P (2004) Introductory quantum optics. Cambridge University Press, Cambridge. ISBN 052152735X
12. Glauber R (1963) Coherent and incoherent states of the radiation field. Phys Rev 131:2766–2788
13. Greiner M (2003) Ultracold quantum gases in three-dimensional optical lattice potentials. PhD thesis, Ludwig-Maximilians-Universität München, München
14. Greiner M, Mandel O, Esslinger T, Hänsch TW, Bloch I (2002) Quantum phase transition from a superfluid to a Mott insulator in a gas of ultracold atoms. Nature 415:39–44
15. Grimm R, Weidemüller M, Ovchinnikov YB (2000) Optical dipole traps for neutral atoms. Adv Atom Mol Opt Phys 42:95–170
16. Haas M, Jentschura UD, Keitel CH (2006) Comparison of classical and second quantized description of the dynamic stark shift. Am J Phys 74:77
17. Hubbard J (1963) Electron correlations in narrow energy bands. Proc R Soc A 276:238–257
18. Huber SD, Altman E, Buchler HP, Blatter G (2007) Dynamical properties of ultracold bosons in an optical lattice. Phys Rev B 75:85106
19. Jaksch D, Bruder C, Cirac JI, Gardiner C, Zoller P (1998) Cold bosonic atoms in optical lattices. Phys Rev Lett 81:3108–3111
20. Kashurnikov V, Svistunov B (1996) Exact diagonalization plus renormalization-group theory: accurate method for a one-dimensional superfluid-insulator-transition study. Phys Rev B 53:11776–11778
21. Kohn W (1959) Analytic properties of bloch waves and wannier functions. Phys Rev 115:809–821
22. Kühner TD, White SR, Monien H (2000) One-dimensional Bose-Hubbard model with nearest-neighbor interaction. Phys Rev B 61:12474–12489
23. Leggett A (2006) Quantum liquids: Bose condensation and cooper pairing in condensed-matter systems. Oxford University Press, USA
24. Menotti C, Trivedi N (2008) Spectral weight redistribution in strongly correlated bosons in optical lattices. Phys Rev B 77:235120
25. I. A. S. Milton Abramowitz (1972) Handbook of mathematical functions with formulas, graphs, and mathematical tables. Dover Publications, New York. ISBN 0486612724
26. Pethick CJ, Smith H (2001) Bose-Einstein condensation in dilute gases. Cambridge University Press, Cambridge
27. Sachdev S (2011) Quantum phase transitions. Cambridge University Press, Cambridge, 2nd edn. ISBN 0521514681
28. Sherson JF, Weitenberg C, Endres M, Cheneau M, Bloch I, Kuhr S (2010) Single-atom-resolved fluorescence imaging of an atomic Mott insulator. Nature 467:68–72
29. Trotzky S, Pollet L, Gerbier F, Schnorrberger U, Bloch I, Prokofev NV, Svistunov B, Troyer M (2010) Suppression of the critical temperature for superfluidity near the Mott transition. Nat Phys 6:998–1004

30. Van Kempen EGM, Kokkelmans SJJMF, Heinzen DJ, Verhaar BJ (2002) Interisotope determination of ultracold rubidium interactions from three high-precision experiments. Phys Rev Lett 88:093201
31. van Oosten D (2004) Quantum gases in optical lattices: the atomic Mott insulator. PhD thesis, Universiteit Utrecht, Utrecht
32. Wannier G (1937) The structure of electronic excitation levels in insulating crystals. Phys Rev 52:191–197
33. Wessel S, Alet F, Troyer M, Batrouni G (2004) Quantum Monte Carlo simulations of confined bosonic atoms in optical lattices. Phys Rev A 70:053615
34. Will S (2011) Interacting bosons and fermions in three-dimensional optical lattice potentials. PhD thesis, Johannes Gutenberg-Universität Mainz, Mainz
35. Zwerger W (2003) Mott-Hubbard transition of cold atoms in optical lattices. J Opt B Quantum Semiclass 5:9–16

http://www.springer.com/978-3-319-05752-1

Probing Correlated Quantum Many-Body Systems at the Single-Particle Level

Endres, M.

2014, XVI, 165 p. 50 illus., 37 illus. in color., Hardcover
ISBN: 978-3-319-05752-1